

Observations and Modeling of Wind-driven Currents in the Northeast Pacific

PATRICK F. CUMMINS AND HOWARD J. FREELAND

Institute of Ocean Sciences, Sidney, British Columbia, Canada

(Manuscript received 10 October 1991, in final form 13 May 1992)

ABSTRACT

Velocity measurements from the interior of the Alaskan gyre are presented from a current meter mooring deployed in 4000 m of water at 49°33'N, 138°38'W, in the vicinity of Ocean Weather Station P. The mooring held five current meters, which spanned the depth of the water column. The data reveal surface-intensified motions with flow fluctuations in the upper layers of the water column characterized by long-period, $O(100 \text{ d})$ time scales of variability. At abyssal depths, the flow displays shorter, $O(20 \text{ d})$ time scales of variability. The data are compared with observations from one of the NEPAC moorings in the northeast Pacific (42°N, 152°W). Similar characteristics in kinetic energy levels, in the vertical structure of the flow, and in the vertical variation of eddy time scales are found at this location.

The current measurements are considered in terms of the linear theory of directly wind-driven variability of Müller and Frankignoul. A comparison with simulated currents from a quasigeostrophic numerical model demonstrates that stochastic atmospheric forcing of the ocean can account for the observed variability. The numerical experiments and a simple extension of the linear theory suggest that the presence of bottom topography is important for the partition of energy between vertical modes and for the vertical variation of the time scales of the flow.

1. Introduction

The large-scale circulation in the eastern North Pacific is dominated by the wind-driven, cyclonic motion of the Alaskan gyre. The exploration of this gyre has been largely concentrated on the Alaskan Stream, the intense boundary current that originates at the head of the Gulf of Alaska and flows westward along the Aleutian Islands. The vast expanse of water found in the interior of the Alaskan gyre is one of the under-explored regions of the World Ocean. Knowledge of circulation properties in the region has been derived mainly from a number of hydrographic surveys and from the long-term hydrographic measurements collected along line P (e.g., Tabata 1991). These data have provided insight into the relative motion of the upper 1000 m of the water column and into the variability of the baroclinic transport of the gyre. Recently, Thomson et al. (1990) utilized satellite-tracked drifter data to infer upper-layer flow statistics.

There have been very few direct current meter measurements from moored instrumentation in the northeast Pacific. As a result, comparatively little is known about absolute flow velocities or the structure of deep currents. In this paper we discuss the results of one of the first attempts to directly measure the currents in

this region. Data from a mooring initially deployed in June 1989 at 49°33'N, 138°38'W are presented. Aside from the present study, we are aware of only one other long-term deep-ocean mooring in the Alaskan gyre, located near the head of the Gulf of Alaska (T. Royer, personal communication). In the following, the velocity data from the 49°33'N, 138°38'W mooring (henceforth, the LP10-1 mooring) are used to investigate the physical mechanisms of eddy variability in the interior of the Alaskan gyre.

For regions such as the Alaskan gyre that are distant from boundary currents and their seaward extensions, theoretical studies suggest that direct atmospheric forcing of the ocean is a plausible eddy generation mechanism. This hypothesis has served as the basis for the analytical studies of Frankignoul and Müller (1979), Willebrand et al. (1980), and Müller and Frankignoul (1981; hereafter MF81). These works have attempted to demonstrate the importance of stochastic wind forcing to producing midocean variability. Recently, indirect evidence for wind-driven variability over the central and eastern North Pacific has been given by Koblinsky et al. (1989), who found a significant seasonal modulation in abyssal eddy kinetic energy levels. As Brink (1989) noted, however, it has generally been difficult to observe "direct" atmospheric forcing of oceanic variability. Attempts to establish a coherence between ocean currents and local wind forcing have proven problematic and the theory explicitly predicts such coherences will be very small (MF81). To overcome these difficulties, Brink developed a

Corresponding author address: Dr. Patrick F. Cummins, Institute of Ocean Sciences, 9860 West Saanich Road, Sidney, V8L 4B2, BC, Canada.

model for the nonlocal coherence between ocean currents and wind forcing. This model, although partially successful at reproducing the spatial coherence pattern, could not account for the observed baroclinicity or energy level of the currents in the North Atlantic.

Recent measurements of depth-averaged velocity from an array of electrometers in the central North Pacific (Luther et al. 1990; Chave et al. 1992) have provided compelling "direct" evidence for wind-forced barotropic currents. The results of these studies conform qualitatively with the theoretical studies of Brink and Samelson (1989) and show significant nonlocal coherence between barotropic currents and the wind-stress curl derived from the Fleet Numerical Oceanographic Center (FNOC) winds. Chave et al. (1992) emphasize the importance of filtering out the baroclinic component of the velocity field in order to establish coherence with the wind forcing. Baroclinic contamination may partially explain the considerably greater coherences of Chave et al. (1992) over those obtained by Brink (1989) and Samelson (1990) from current meter measurements.

Due to the presence of an important baroclinic component in the currents of the northeast Pacific, a different, "indirect" approach to modeling the variability of currents at LP10-1 is adopted here. This approach is based on an intercomparison between the observations and simulated currents obtained from a quasigeostrophic numerical model, which focuses on the vertical structure and energy levels of the currents. In contrast to previous models, a reasonably satisfactory agreement between observed and modeled kinetic energies and vertical structure is obtained. The intercomparison also provides evidence of the atmospheric forcing of low-frequency baroclinic motions and demonstrates that in the northeast Pacific mesoscale fluctuations in the wind field can produce significant currents throughout the water column.

In the next section, the salient characteristics of the LP10-1 data are discussed and compared with data from the NEPAC mooring at 42°N, 152°W. Velocity data from these two moorings are shown to have comparable energy levels and a similar partition of barotropic and baroclinic kinetic energy. In section 3a the linear theory of wind driven variability over a stratified ocean with a uniformly sloping bottom is considered. Finally, the linear theory is used to interpret the vertical structure of the observations and of simulated currents from several quasigeostrophic numerical experiments, discussed in section 3b.

2. Observations

The LP10-1 mooring was first deployed in June 1989 and has since been serviced on several occasions. In the following analysis we will be concerned with data from the first three deployments, a duration of about one year. The water depth at the mooring site is

3980 m and the local bottom topography is relatively flat and smooth. The mooring carried Aanderaa RCM4 current meters at nominal depths of 200 m, 600 m, and 1500 m, and Aanderaa RCM5 current meters at 2200-m and 3000-m depths. The top float was a few meters above the shallowest current meter, near 200-m depth. The depths of current meters were determined by a condition to provide optimal separation of the barotropic and first three baroclinic modes. The shape of these modes was determined from historical averages of density observed at station 10 along line P (49°34'N and 138°40'W), about 3 km away from the mooring site (see Tabata and Peart 1986). The first three modes are illustrated in Fig. 1; also marked on the figure are the nominal depths of the five current meters. The modes were recomputed using summer and winter data at station 10 and it was found that the modal shapes were quite insensitive to the small density changes. Thus, in the subsequent analysis, the decomposition into modes is based on those resulting from the climatological mean data at station 10.

During the first deployment, only four out of the five instruments deployed actually functioned. This resulted in the separation of the current observations into modal amplitudes being suboptimal. In the subsequent two deployments, the failures were even greater and, in particular, no data were acquired from the current meter at 200 m. Thus, it was decided that modal separations for those deployments should not be done. Current meter data for the first year are shown in Fig. 2. The first deployment includes 131 days of data, during which time the instrument at 200 m was functioning. The current velocities were sampled at half-hour intervals and have been filtered with a Lanczos cosine filter, which has a half-power point at a period of 40 h. This filter has a very steep frequency-response curve and effectively eliminates all energy in the diurnal tidal band, but leaves signals with a period of 2 days virtually unaltered. During the filter operation, the data were subsampled at one-half day intervals, and all of these subsamples are displayed in Fig. 2.

Casual inspection of Fig. 2 reveals some of the important properties of the currents. Velocities are largest near the surface and decrease steadily with increasing depth. The currents in the upper water column are heavily dominated by a low-frequency signal with a period longer than the sampling period defined by these records. As we move lower in the water column, the low-frequency signal is gradually replaced by high-frequency variations until at a depth of 3000 m the near-surface, low-frequency variability apparently disappears entirely.

Spectra of currents from 600 and 3000 m are presented in Fig. 3. At higher frequencies the currents at the two depths have effectively indistinguishable spectra. At the lowest resolved frequencies the energy is higher at the shallower level by about a factor of 2-3. This excess of low-frequency energy is evident in Fig.

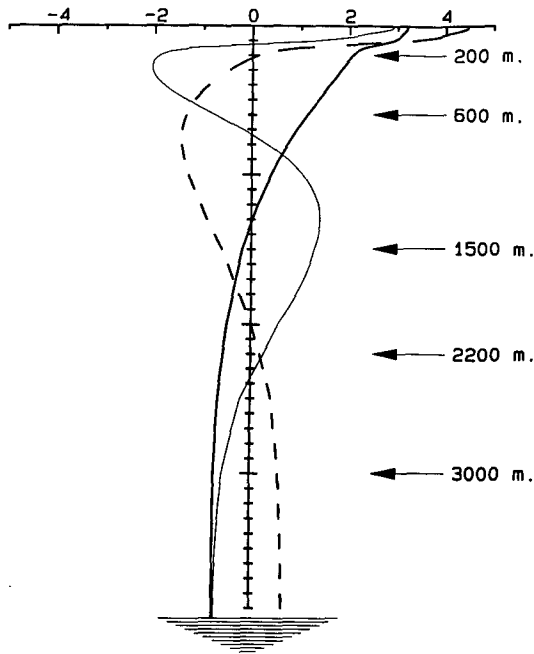


FIG. 1. The vertical distribution of the first three horizontal velocity wave modes computed from climatological mean density data from station 10 along line P (49°34'N and 138°40'W; Tabata and Peart 1986).

2; however, the length of the record does not appear to be adequate to describe the difference between the spectra at the low frequencies. The spectra of Fig. 3 are similar in several respects to the spectra of depth-averaged currents from site EC in the central North Pacific presented by Chave et al. (1992). These have a comparable roll-off between 0.01 and 0.1 cpd and a similar “shoulder” at periods of a few days. Energy levels are also comparable.

The variation in time scales with depth is more readily evident in Fig. 4, where we plot the temporal structure function for the north-south component of velocity $v(t)$ of each time series. The structure function is defined by

$$b(\tau) = \frac{\overline{[v(t + \tau) - v(t)]^2}}{\overline{v(t)^2}}, \quad (2.1)$$

where the overbar denotes a time average. The time scale needed to reach a saturation value (twice the variance) gives an indication of the dominant time scale underlying the time series. As we move steadily deeper in the water column, the time series are increasingly dominated by processes occurring at steadily shorter time scales; a time scale of 20–25 days is dominant at 3000 m.

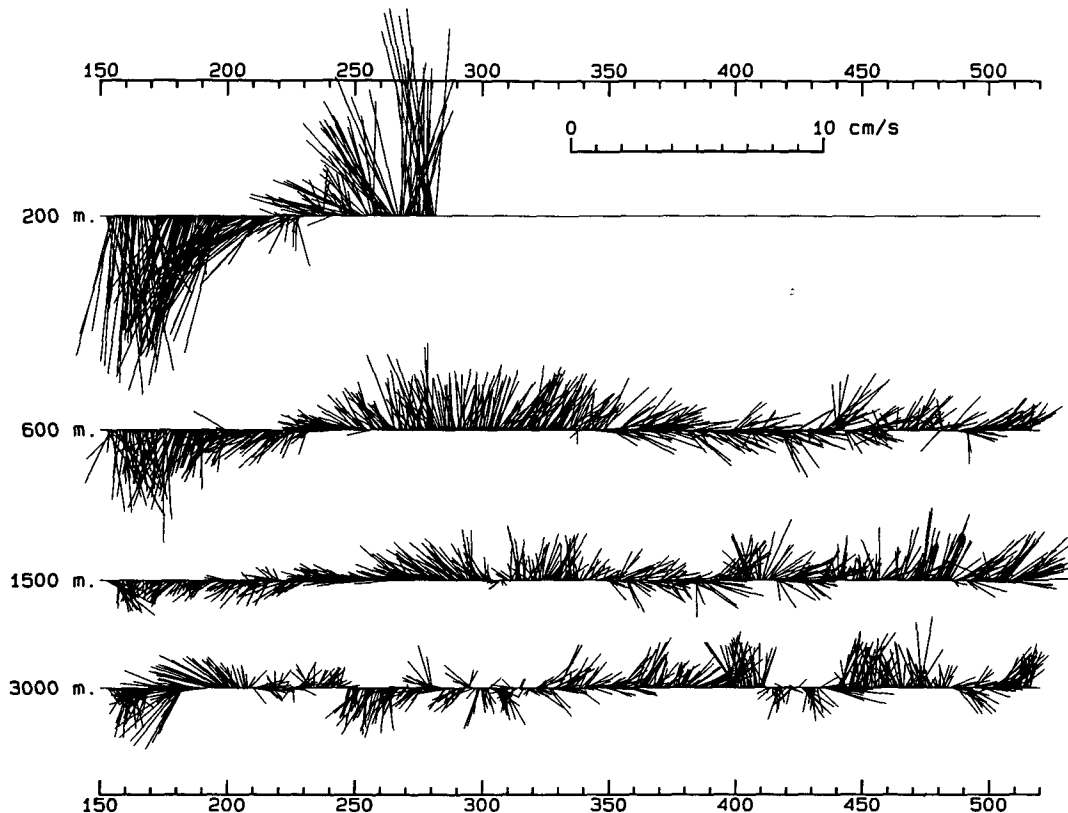


FIG. 2. Stick plots at one-half day intervals of the low-passed currents from mooring LP10-1. The time axis indicates the day number of 1989; day 150 is 30 May.

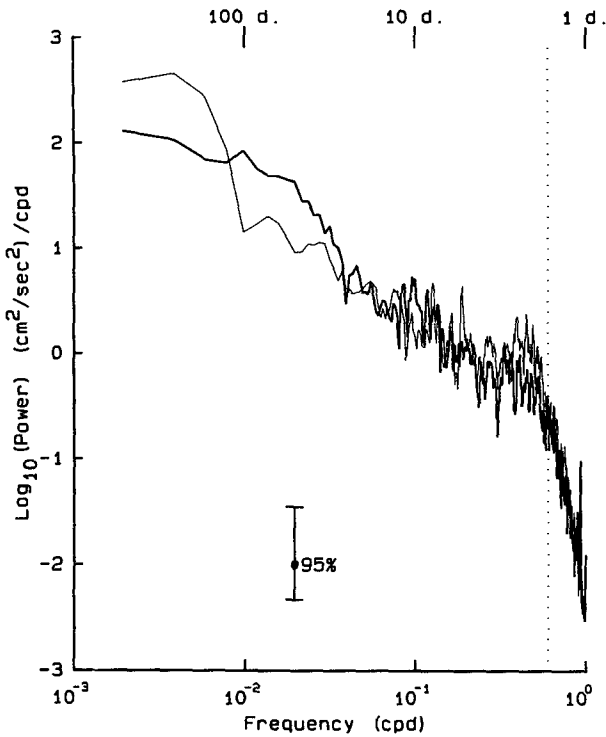


FIG. 3. Power spectra of currents at 600- and 3000-m depth (light and bold lines, respectively). Each spectral estimate has 8.6 degrees of freedom. The dotted line indicates the frequency above which the effects of the low-pass filter become significant.

Table 1 lists a few basic statistics computed from the four velocity time series at the LP10-1 mooring. In constructing this table the usual definition of eddy kinetic energy, K_E , has been adopted

$$K_E = \frac{1}{2} \overline{(u'^2 + v'^2)}, \quad (2.2)$$

where $(u', v') = (u - \bar{u}, v - \bar{v})$. Note that the statistics at 200 m are based on only four months of data. The kinetic energies in the deep water are very small, but

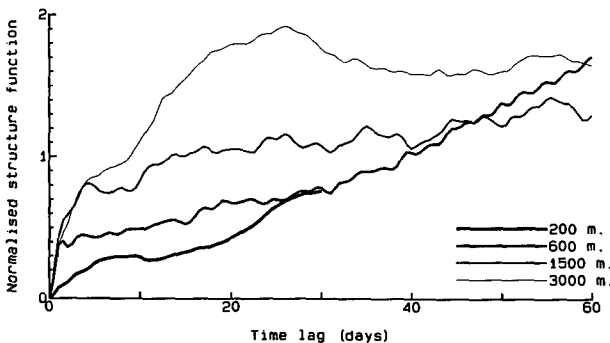


FIG. 4. Temporal structure functions of the meridional component of velocity at different depths from the LP10-1 mooring.

they are measurable with the instrumentation used. These statistics are based on low-passed data; rms tidal signals of around $8-10 \text{ cm s}^{-1}$ were removed by the low-pass filter and these signals were sufficient to guarantee that current speeds were almost always above the threshold for Aanderaa RCM4 and RCM5 current meters. As the statistics of Table 1 indicate, means are very small at all depths including the 200-m level, and the eddy kinetic energy levels decrease steadily with depth.

As mentioned earlier, the separation into vertical modes will be carried out only for the first deployment, that is, the first 131 days of low-pass filtered data. These modes are solutions to the eigenvalue problem (3.2) with boundary conditions (3.3), given below, and are normalized according to (3.4). Expanding the E/W component of velocity as

$$u(z, t) = \sum_{i=0}^{\infty} F_i(z)A_i(t), \quad (2.3)$$

we derive the equation for the amplitude time series associated with the i th mode $A_i(t)$ as:

$$A_i(t) = \frac{1}{H} \int_0^H u(z, t)F_i(z)dz. \quad (2.4)$$

The continuous variation of u with z and time is not known, so we approximate the above integral with

$$A_i(t) = \frac{1}{H} \sum_{j=1}^N u_j(t)F_i^j \Delta z_j, \quad (2.5)$$

where N is the number of current meters used in the expansion and F_i^j is the value of the i th mode evaluated at depth z_j , that is, the depth of the j th current meter; $u_j(t) = u(z_j, t)$; and Δz_j is a weighting function, specifically the depth interval represented by the j th current meter. The same analysis can, of course, be used to expand the N/S component of velocity into an amplitude time series, $B_i(t)$.

Using the above analysis technique, it is a simple matter to compute the amplitude time series and estimate the kinetic energy accounted for by each mode. Since we have only four functional current meters, the velocities were analyzed into three modes only, the barotropic and the first two baroclinic modes. The loss

TABLE 1. Statistics of low-passed filtered currents from the LP10-1 mooring. The mean velocities \bar{u} and \bar{v} are given in cm s^{-1} , while the units of $\overline{u'^2}$, $\overline{v'^2}$, and K_E are $\text{cm}^2 \text{s}^{-2}$. The final column indicates the number of days of data used to compute each average.

Depth (m)	\bar{u}	\bar{v}	$\overline{u'^2}$	$\overline{v'^2}$	K_E	Period (days)
200	-1.1	-0.8	1.5	12.3	6.9	131
600	0.3	0.2	1.2	1.5	1.3	365
1500	0.1	0.1	1.0	0.6	0.8	365
3000	0.1	0.2	0.8	0.8	0.8	365

of data from the 2200-m level results in the estimation procedure being suboptimal. The covariance matrix of the vertical wave modes in the frame of reference of the sampling scheme is defined as $\text{cov}_{i,j}$, where

$$\text{cov}_{i,j} = \frac{1}{H} \sum_{k=1}^N F_i^k F_j^k \Delta z_k, \quad (2.6)$$

and the correlation matrix $C_{i,j} = \text{cov}_{i,j} / [\text{cov}_{i,i} \text{cov}_{j,j}]^{1/2}$. For the specific sampling considered here, and for the specific modes analyzed, the correlation matrix is

$$C_{i,j} = \begin{pmatrix} 1.0 & 0.03 & -0.18 \\ 0.03 & 1.0 & -0.54 \\ -0.18 & -0.54 & 1.0 \end{pmatrix}.$$

Thus, we see that the orthogonality of the barotropic and first baroclinic mode has, fortunately, been maintained, as has that between the barotropic and second internal mode. The first and second internal modes correlate more than they should, however. This implies that we can realistically estimate the amplitude of the barotropic mode, but the separation of the first two baroclinic modes could be better. In fact, a correlation of 0.54 is not particularly high; for two independent processes correlated by that amount we would conclude that they have only 25% of their total variance in common. So the separation, though definitely suboptimal, is not bad. We must anticipate, however, that some energy computed as being mode-2 energy might actually be mode-1 energy, and vice versa.

The separation into three modes places 50% of the fitted kinetic energy in the barotropic mode, 40% in the first baroclinic mode, and only 10% in the second baroclinic mode, while 18% of the total energy remains unaccounted for in the fit. Using the modal decomposition we can estimate the depth-averaged kinetic energy as

$$\begin{aligned} E_{KE} &= \frac{1}{H} \int_0^H \frac{1}{2} (\overline{u'^2 + v'^2}) dz \\ &= \frac{1}{2} \sum_{n=0}^N (\overline{A_n^2 + B_n^2}) + \text{residual}, \quad (2.7) \end{aligned}$$

which yields an estimate of the kinetic energy as $1.3 \text{ cm}^2 \text{ s}^{-2}$. The amount of energy in mode 2 is very small, so it appears that the possible leakage of energy from mode 2 to mode 1 is not a serious problem.

Comparison with NEPAC observations

The NEPAC current meter data consists of about three years of observations collected during the mid-1980s from two moorings in the northeast Pacific at 28°N and 42°N , 152°W . A complete presentation of the data is contained in the report by Hu and Niiler (1987). In the following we consider the first two years of data from the 42°N mooring; this is the closest deep-ocean mooring to the LP10-1 site, an indication of the

sparsity of data coverage in the northeast Pacific. Results from this mooring were also presented by Koblinsky et al. (1989). The mooring was deployed in consecutive years, 1982 and 1983; however, since the depths of instruments varied significantly from one year to the other, it was not possible to merge the datasets into a two-year long time series. For this reason we will examine these two deployments independently. We also neglect the third year of data because the instrumental problems noted in Hu and Niiler (1987) make much of the deep velocity measurements suspect during this last deployment.

The mooring on the first deployment carried seven instruments at depths of 80, 156, 281, 405, 606, 956, and 3756 m, and on the second deployment the mooring carried ten instruments at nominal depths of 95, 145, 196, 270, 345, 444, 569, 896, 1196, and 3980 m. One of the instruments in the first deployment, at 606 m, failed about 20 days before recovery, with the result that the total amount of low-passed data available for modal analysis is 333 days in the first deployment and 298 days in the second deployment. The data were low-pass filtered and subsampled in a manner identical with the treatment of the LP10-1 data discussed earlier. The depth distribution of K_E is given in Table 2. The magnitude of K_E and the variation with depth is similar to the observations at LP10-1. At abyssal depths rms currents are about 1 cm s^{-1} at both locations.

The NEPAC data were subjected to a modal decomposition similar to the LP10-1 data in order to extract the barotropic and first two baroclinic modes. The modes were computed from the climatological Levitus data for a 1° square about the mooring site. For the first year NEPAC deployment, the separation appears to be efficient; the largest off-diagonal element in the modal correlation matrix is -0.19 between internal modes 1 and 2. The separation into three modes accounts for 95% of the variance in the system; of the fitted energy 58%, 28%, and 14% is in the barotropic, first internal, and second internal modes, respectively. The depth-integrated kinetic energy estimated from the modal decomposition is $1.46 \text{ cm}^2 \text{ s}^{-2}$. For the second-year NEPAC deployment, we are dealing with a very dense array of current meters, though the sampling in the deep water is, perhaps, a little coarse. In this case the largest off-diagonal element of the modal correlation matrix is only -0.21 . The decomposition into three modes leaves a residual of only 8% of the variance. Of the fitted energy, 39%, 46%, and 15% fall into the barotropic, first internal, and second internal modes, respectively, and the modal decomposition implies a depth-integrated kinetic energy close to that of the first year, $1.53 \text{ cm}^2 \text{ s}^{-2}$.

A summary of the modal decompositions at the LP10-1 and NEPAC moorings is given in Table 3. The two NEPAC deployments give the nearly same estimate of depth-integrated eddy kinetic energy, and show that the barotropic and first baroclinic modes

TABLE 2. Eddy kinetic energy in $\text{cm}^2 \text{s}^{-2}$ of low-passed filtered currents from approximately two years of data from the NEPAC mooring at 42°N , 152°W . Year 1 covers the period July 1982–July 1983, while year 2 is for July 1983–May 1984.

Year 1		Year 2	
Depth (m)	K_E	Depth (m)	K_E
70	15.2	43	24.8
146	7.8	93	16.5
271	4.5	144	13.1
395	3.6	218	10.7
596	2.3	293	7.1
946	1.6	392	4.9
3746	0.8	517	4.1
		844	1.7
		1144	1.3
		3928	0.6

account for most of this energy. Furthermore, the results from the NEPAC mooring are very similar to the results from the LP10-1 mooring discussed above.

The NEPAC data also show similarity with LP10-1 in the variation of the time scales of flow with depth and in the absence of a coherence between deep- and upper-ocean currents. In Fig. 5 we show the structure functions calculated for the second-year NEPAC data for current meters at depths of 196, 569, 1196, and 3980 m (chosen to approximate the location of instruments used in Fig. 1 for the line-P mooring). Clearly the deep instruments approach the saturation value of 2 in 10–15 days; however, with the largest lag plotted of 60 days, it is clear that the shallow instruments have not even approached the saturation value yet. The dominant time scale at 200 or 600 m remains undefined.

3. Modeling the observations

As a first step to model the observations, coherence maps were constructed, similar to those of Chave et al. (1992), between the two components of velocity at 3000 m from LP10-1 and atmospheric variables (wind stress curl and surface pressure) derived from the FNOC product. Regions of significant coherence were found in high-frequency (3.5–11 day period) and low-frequency (>30 day period) bands, providing some evidence for direct atmospheric forcing at this site.

TABLE 3. The depth-integrated eddy kinetic energy (E_{KE}) in $\text{cm}^2 \text{s}^{-2}$ and the partition of E_{KE} among the vertical modes from the LP10-1 and NEPAC (first and second year) moorings. The last column gives the averaging period in days.

E_{KE}	Percent			Residual	Period
	Mode 0	Mode 1	Mode 2		
LP10-1	1.30	50	40	10	18
NEPAC-Y1	1.46	58	28	14	5
NEPAC-Y2	1.53	39	46	15	8

Aside from this fact, the coherence calculations present problems of interpretation and appear to be relatively uninformative. The coherent regions are not consistently manifested in the two components of velocity. In addition, the coherence pattern and amplitude are difficult to relate to the theoretical models.

Due in part to these difficulties, a different “indirect” approach to modeling the observations is discussed below. First, the linear theory of directly wind-driven variability in a layered quasigeostrophic ocean with a mean bottom slope is considered. This theory is then applied to interpret simulated currents derived from numerical experiments with a multilayer quasigeostrophic model. The results of the numerical experiments support the contention that the stochastic forcing by the atmosphere is the driving mechanism for the observed variability. The results also suggest that the presence of bottom topographic variations has an important influence on the vertical structure of the oceanic response in this region.

a. Linear theory

To interpret the numerical results presented in section 3c, it is useful to consider the linear response of an unbounded, quasigeostrophic ocean to a fluctuating wind. In this section a relation between the oceanic frequency spectrum and the forcing wind-stress curl spectrum is derived and used to examine the qualitative aspects of the response of the ocean to stochastic forcing in the presence of a simple bottom topography. The development is similar to that of MF81, but allows for the effects of a mean bottom slope. Since one of the main characteristics of the bathymetry of the northeast Pacific is a gentle shoaling to the northeast, a mean bottom slope may be considered a very simple idealization of the topography of this region. Rhines (1970) considered the influence of a bottom slope on the ver-

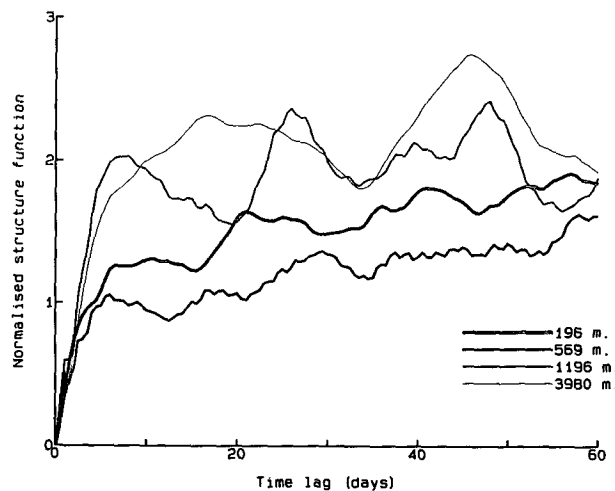


FIG. 5. Temporal structure functions of the zonal component of velocity at three different depths during the second year at the NEPAC mooring (42°N , 152°W).

tical structure of free Rossby waves in a channel. Samelson (1989) has examined the effects of a sloping bottom on remote coherences in a two-layer model. Here we consider the influence on the vertical structure of the forced response.

For a layered quasigeostrophic ocean, the relation between the layer streamfunction $\psi_k(x, y, t)$ and the modal streamfunction $\phi_m(x, y, t)$ is given by

$$\psi_k = \sum_{m=0}^M F_m^k \phi_m, \quad (3.1)$$

where m is the mode index, and k is the layer index with $k = 0$ denoting the uppermost layer and $k = M$, the bottom layer. The F_m^k are the eigenvectors or normal modes of a discretized form of the Sturm-Liouville equation,

$$\frac{\partial}{\partial z} \left(\frac{f_0^2}{N^2} \frac{\partial F_m}{\partial z} \right) + \lambda_m^2 F_m = 0, \quad (3.2)$$

where the eigenvalue, λ_m^2 , is the reciprocal of the square of the Rossby deformation radius of mode m , and f_0 is the local Coriolis parameter. Boundary conditions are for no vertical displacement at the bottom ($z = -H$) and at the surface ($z = 0$)

$$\frac{\partial F_m}{\partial z} = 0, \quad z = 0, -H. \quad (3.3)$$

The eigenfunctions are normalized such that

$$H^{-1} \int_{-H}^0 F_m F_n dz = \delta_{m,n}. \quad (3.4)$$

In a standard coordinate system, the linearized equation governing the evolution of the modal streamfunction (e.g., Flierl 1978) is

$$\begin{aligned} \frac{\partial}{\partial t} (\nabla^2 - \lambda_m^2) \phi_m + \beta \frac{\partial \phi_m}{\partial x} \\ = \frac{F_m^0 W}{\rho_0 H} - R \nabla^2 \phi_m - \frac{F_m^M}{H} \sum_j F_j^M J(\phi_j, f_0 h), \end{aligned} \quad (3.5)$$

where β is the meridional gradient of the Coriolis parameter; F_m^0 and F_m^M are the amplitudes of vertical mode m at the surface and bottom layers, respectively; $W = \mathbf{k} \cdot \nabla \times \boldsymbol{\tau}$ is the wind-stress curl; h is the deviation of the bottom from the mean depth H ; and $J(a, b) = a_x b_y - b_x a_y$ is the Jacobian operator. As in MF81, a simple Rayleigh damping term with a decay time scale of R^{-1} is used to model dissipation and transfer mechanisms. The last term in (3.5) includes the effects of modal coupling due to bottom topographic variations. To simplify this term, attention is restricted to a mean bottom slope such that $h(x, y) = s^x x + s^y y$, where (s^x, s^y) are the bottom slopes in the east-west and north-south directions, respectively.

We assume that ϕ_m and W can be expanded as sums of Fourier components of the form

$$\phi_m = \text{Re}[\hat{\phi}_m(\boldsymbol{\kappa}, \omega) \exp[i(\boldsymbol{\kappa} \cdot \mathbf{x} - \omega t)]], \quad (3.6)$$

where $\boldsymbol{\kappa} = (k_1, k_2)$ is the horizontal wavenumber vector and ω is the angular frequency. Substituting (3.6) into (3.5) yields a relation between the oceanic response and the wind forcing,

$$\begin{aligned} i \hat{\phi}_m [(\omega - \omega_m)(k^2 + \lambda_m^2) + ik^2 R] \\ + i F_m^M (T^y k_1 - T^x k_2) \sum_j F_j^M \hat{\phi}_j = \frac{F_m^0}{\rho_0 H} \hat{W}, \end{aligned} \quad (3.7)$$

with $(T^x, T^y) = (f_0 s^y / H, f_0 s^x / H)$. The resonance frequencies ω_m satisfy the dispersion relation for free waves, $\omega_m = -\beta k_1 / (k^2 + \lambda_m^2)$, with $k^2 = \boldsymbol{\kappa} \cdot \boldsymbol{\kappa}$.

Adopting the notation, $\Omega_m = (\omega - \omega_m)(k^2 + \lambda_m^2)$ and $T = T^y k_1 - T^x k_2$, (3.7) can be put in matrix form as

$$\mathbf{A}(\hat{\phi}_m) = -i \frac{\hat{W}}{\rho_0 H} (F_m^0), \quad (3.8)$$

where $(\hat{\phi}_m) = (\hat{\phi}_0, \hat{\phi}_1, \dots, \hat{\phi}_M)^T$ and $(F_m^0) = (F_0^0, F_1^0, \dots, F_M^0)^T$ are column vectors and

$$\mathbf{A} = \begin{pmatrix} \Omega_0 + TF_0^M F_0^M + iRk^2 & TF_0^M F_1^M & & TF_0^M F_M^M \\ TF_1^M F_0^M & \Omega_1 + TF_1^M F_1^M + iRk^2 & & TF_1^M F_M^M \\ & & \dots & \\ TF_M^M F_0^M & TF_M^M F_1^M & & \Omega_M + TF_M^M F_M^M + iRk^2 \end{pmatrix}.$$

The solution to (3.8) is then $(\hat{\phi}_m) = (X_m) \hat{W} / \rho_0 H$, where $(X_m) = -i \mathbf{A}^{-1} (F_m^0)$ is the transfer function of each mode.

The frequency-wavenumber spectrum of the wind forcing is defined as

$$E_W(\boldsymbol{\kappa}, \omega) = \frac{\langle \hat{W}(\boldsymbol{\kappa}, \omega) \hat{W}^*(\boldsymbol{\kappa}, \omega) \rangle}{2\Delta\boldsymbol{\kappa}\Delta\omega}, \quad \omega \geq 0 \quad (3.9)$$

where angle brackets and the asterisk denote an ensemble average and the complex conjugate, respectively. Similarly, the kinetic energy spectrum of the oceanic response is given by

$$E_K^m(\boldsymbol{\kappa}, \omega) = \frac{1}{2} \rho_0 k^2 \frac{\langle \hat{\phi}_m(\boldsymbol{\kappa}, \omega) \hat{\phi}_m^*(\boldsymbol{\kappa}, \omega) \rangle}{2\Delta\boldsymbol{\kappa}\Delta\omega}, \quad \omega \geq 0. \quad (3.10)$$

Substituting for $\hat{\phi}_m$ in (3.10), we have

$$E_K^m(\kappa, \omega) = \frac{1}{2} \rho_0^{-1} H^{-2} k^2 (X_m)^T (X_m^*) E_W(\kappa, \omega), \tag{3.11}$$

which relates the oceanic response to the frequency-wavenumber spectrum of the wind forcing. The kinetic energy in each mode is obtained by integrating over wavenumber and frequency,

$$E^m = \int \int \int E_K^m(\kappa, \omega) dk_1 dk_2 d\omega. \tag{3.12}$$

Before considering the effects of topography, it is instructive to consider the vertical structure in the flat-bottom case. With $T = 0$, the matrix \mathbf{A} is diagonal and the modes are uncoupled. In this case, the ratio of kinetic energy residing in mode m to that in mode n is given by

$$r_{m,n}(\kappa, \omega) = \frac{E_K^m}{E_K^n} = \left(\frac{F_m^0}{F_n^0} \right)^2 \frac{[(\omega - \omega_n)^2 (k^2 + \lambda_n^2)^2 + (Rk^2)^2]}{[(\omega - \omega_m)^2 (k^2 + \lambda_m^2)^2 + (Rk^2)^2]}. \tag{3.13}$$

For $r_{0,1}$, the ratio of the barotropic to first baroclinic mode, (3.13) may be simplified by noting that for the barotropic mode, $\lambda_0 = 0$ (the rigid-lid approximation) and for the baroclinic modes, $k^2 \ll \lambda_m^2$ for $m \geq 1$, assuming that the dominant forcing scales are much larger than the internal deformation radii. Two limits are of particular interest; in the low-frequency limit ($\omega \ll \omega_0, \omega_1$), the ratio of modal amplitudes is

$$r_{0,1} |_{\omega \ll \omega_0, \omega_1} \approx \left(\frac{F_0^0}{F_1^0} \right)^2. \tag{3.14}$$

For the vertical modes at LP10-1 given in Fig. 1, $F_0^0/F_1^0 = 1/3.2$, which implies that a low-frequency or quasi-steady forcing produces a predominantly baroclinic response in the ocean. Due to the distribution of the first vertical mode, this response is surface intensified.

In the high-frequency limit ($\omega \gg \omega_0, \omega_1 > R$), (3.13) reduces to

$$r_{0,1} |_{\omega \gg \omega_0, \omega_1} \approx \left(\frac{F_0^0}{F_1^0} \right)^2 \frac{\lambda_1^2}{k^2} \gg \left(\frac{F_0^0}{F_1^0} \right)^2. \tag{3.15}$$

The inequality holds by virtue of the previous assumption on the scales of the forcing. The barotropic mode dominates the high-frequency response. Willebrand et al. (1980) point out that in a flat-bottom ocean the response is barotropic for periods shorter than 300 days. The distribution of the vertical modes is such that, given equal modal amplitudes, barotropic mode fluctuations dominate near the bottom ($F_0^M/F_1^M = 1/$

0.77). The barotropic response to high-frequency forcing should dominate the lower layers of the water column. In addition, a reduction in the scale of the wind forcing will lead to an increase in the amplitude of the first baroclinic mode relative to the barotropic mode.

Bottom topography affects vertical structure of the wind-driven oceanic response in several ways. By coupling modes, a direct topographic energy transfer between modes is possible. For the sloping bottom problem, this effect is due to the off-diagonal terms in the coupling matrix \mathbf{A} . In addition, topography can alter the energy transfer from the forcing to each mode, for example, by modifying the diagonal terms in \mathbf{A} . Finally, in nonlinear problems, topography can have an important influence on the nonlinear energy transfer between modes (e.g., Rhines 1977). In numerical simulations of wind-forced flow over a rough-bottom topography, Treguier and Hua (1989) observed that topography tended to increase the baroclinicity of the flow and to produce a more surface-intensified response.

We use an idealized wind-stress curl spectrum, similar to the one specified by MF81, to examine the effects of a mean bottom slope on the wind-forced response. The wind-stress curl spectrum is given by

$$E_W(\kappa, \omega) = W_0 G(k), \tag{3.16}$$

where $G(k) = G_0$ for $2\pi/L_{\min} \leq k \leq 2\pi/L_{\max}$, and the condition $\iint G(k) dk_1 dk_2 = 1$ determines G_0 . The forcing spectrum is isotropic with the white noise level W_0 assigned a representative value of $2 \times 10^{-7} [\text{N m}^{-3}]^2 \text{ Hz}^{-1}$. The idealized forcing is uniform over length scales ranging from 5000 km to 200 km. The spectra given by (3.11) are integrated numerically to obtain frequency spectra and the total kinetic energy. For simplicity, results are restricted to a two-mode truncation. This was verified to be adequate; since the forcing is cut off at a scale of 200 km, very little energy resides in the higher baroclinic modes, even in the sloping bottom cases.

Frequency spectra of the barotropic and first baroclinic modes for different values of the slope parameters (T^x, T^y) are presented in Fig. 6a,b. The barotropic flat-bottom spectrum has a resonant range for frequencies below the maximum resonant frequency at about 1/6.5 cpd. The sloping topography effectively extends the resonant range to higher frequencies than the flat-bottom cutoff. In addition, the topography partially suppresses the barotropic mode over a range of periods between 30 and 500 days. Some tests with the off-diagonal terms in \mathbf{A} set arbitrarily to zero show that the modifications introduced by the bottom slope for periods shorter than 250 days are almost entirely the result of changes in the direct transfer from the forcing to each mode. The off-diagonal terms have an important influence in reducing the energy of the

baroclinic mode for periods between 250 and 500 days (Fig. 6a,b).

The ratio of baroclinic to barotropic mode frequency spectra as a function of frequency for various values of the bottom-slope parameters is given in Fig. 6c. It is clear that one of the main effects of the bottom slope is to shift to shorter periods the range frequencies over which baroclinic motions are important. The importance of baroclinic motions for periods ranging between 500 and 150 days increases significantly. In the context of a layer model, the relative increase in the low-frequency baroclinic energy will be most evident in the near-surface layers where this mode dominates.

The energy distribution among modes, for various values of the bottom slope and Rayleigh friction, is given in Table 4. These results show that, in both flat and sloping bottom cases, energy levels are approximately inversely proportional to the Rayleigh friction, but baroclinicity, as measured by the energy ratio of between modes, is relatively insensitive to this parameter. A mean meridional slope increases this ratio, while zonal slopes have little effect. Given a nominal value

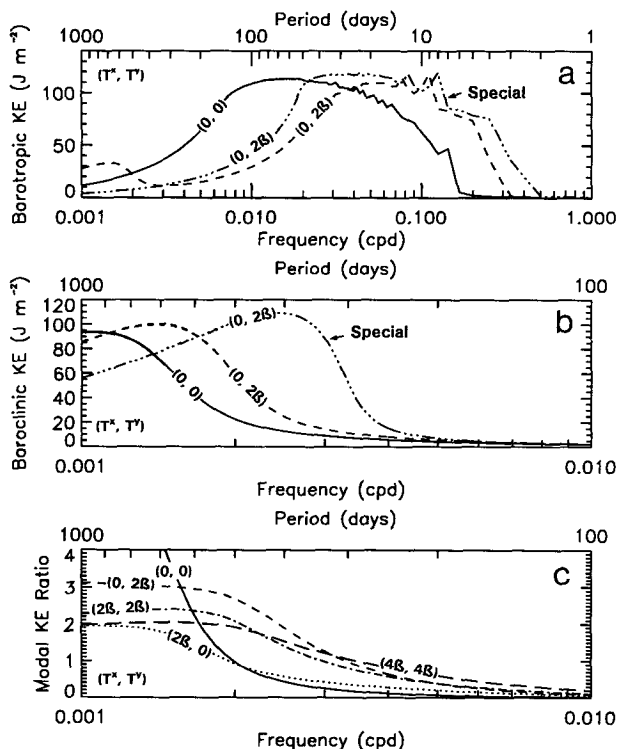


FIG. 6. Variance-preserving kinetic energy spectra of the barotropic (a) and baroclinic (b) mode responses, computed numerically from (3.11) for different values of the topographic slope parameters (T^x , T^y). The Rayleigh friction is $1 \times 10^{-7} \text{ s}^{-1}$ and modal parameters values appropriate to the LP10-1 location were chosen. The roughness of the barotropic spectra at high frequency is a numerical artifact due to finite resolution of the spectral grid of the computation. The curves denoted "special" are spectra computed with the off-diagonal coupling terms in the matrix \mathbf{A} arbitrarily set to zero. The ratio of baroclinic mode to the barotropic mode spectra is given in (c).

TABLE 4. Linear calculation of energy density (J m^{-3}) residing in the barotropic (E^0) and the first baroclinic mode (E^1) as a function of the topographic slope parameters (T^x , T^y) and the Rayleigh friction R . The integration over frequency in (3.12) is restricted to periods between 1 and 1200 days. The ratio in the last column is a measure of the baroclinicity of the response.

(T^x, T^y)	E^0	E^1	E^1/E^0
$R = 1 \times 10^{-7} \text{ s}^{-1}$			
(0, 0)	0.58	0.11	0.20
(0, 2β)	0.56	0.16	0.29
(2β , 0)	0.61	0.12	0.20
(2β , 2β)	0.59	0.15	0.25
$R = 2 \times 10^{-8} \text{ s}^{-1}$			
(0, 0)	2.84	0.55	0.20
(0, 2β)	2.60	0.77	0.30
(2β , 0)	2.93	0.59	0.20
(2β , 2β)	2.94	0.72	0.25

for the Rayleigh friction of $1 \times 10^{-7} \text{ s}^{-1}$ and a bottom slope of $(T^x, T^y) = (0, 2\beta)$, the rms velocity is 3.7 cm s^{-1} . This exceeds, by a factor of about two, the depth-integrated rms velocities of $1.6\text{--}1.8 \text{ cm s}^{-1}$ from the LP10-1 and NEPAC moorings. Brink (1989) has noted the importance of sidewall boundaries in reducing the strength of the response to stochastic forcing from the case of an unbounded ocean.

b. Numerical simulations with a quasigeostrophic model

Simulated currents were generated from a set of numerical experiments and compared with the observed currents described in section 2 in an attempt to identify the important processes for the maintenance of the variability and the vertical structure of the flow in the Alaskan gyre. The simulated currents were obtained from an eddy-resolving, multilayer quasigeostrophic model of the subpolar North Pacific. The model is formulated in spherical coordinates and represents the subarctic region of the North Pacific, from 40° to 60°N , with a realistic coastline geometry. The resolution is $1/6^\circ$ in the zonal and meridional directions and three layers in the vertical are specified. The layer thicknesses are 200 m, 600 m, and 4200 m, while the reduced gravities between the layers are 1.5×10^{-3} and $0.5 \times 10^{-3} \text{ m s}^{-2}$. Although the three-layer structure of the model is a crude approximation to the continuous stratification of the northeast Pacific, the model does give realistic values for the deformation radii and for the amplitude of the first baroclinic mode at the surface. The bottom topography used in some of the experiments is derived from a slight smoothing of the ETOPO5 topographic data (National Geophysical Data Center 1987) and is illustrated in Fig. 1 of Cummins (1991). The model includes a Laplacian friction with a viscosity of $200 \text{ m}^2 \text{ s}^{-1}$ and a linear bottom friction with a decay time scale of 115 days. The value of

the viscosity is the smallest one consistent with the resolution of the model. Details of the mathematical formulation and numerics of the model are omitted here, as they are similar to those of the Cartesian coordinate quasigeostrophic model described in Cummins and Mysak (1988). The model is capable of representing the prominent features of the wind-driven circulation in the subarctic Pacific. Illustrated in Fig. 7 is an instantaneous snapshot of the upper-layer streamfunction from experiment FNOC-T (described below). The signatures of the Alaskan gyre and of the intense boundary current representing the Alaskan Stream are evident on the eastern side of the basin.

For each numerical experiment, the model was integrated in time to a statistically stationary equilibrium before data were stored for analysis. Velocity time-series data at the model point corresponding to (49°30'N, 138°40'W), the one nearest to the mooring coordinates, were recorded at each time step for two to six years of simulated time, depending on the experiment. Tests were conducted to verify that time series from neighboring grid points yield similar results.

The simulated velocity time series were used to determine K_E levels, the partition of K_E between modes, and the vertical variation of the dominant eddy time scales. The averaging period used in the analysis of the model results is generally longer than any available observational record in the northeast Pacific. The dominant time scales of the upper layer in certain experiments require that averages be taken over a few years in order to obtain estimates of the modal K_E partition that are stable to within a few percent. The results from the LP10-1 and NEPAC moorings discussed in section 2 do not, of course, have a comparable accuracy. They do, however, consistently indicate that the barotropic and first baroclinic modes each have a substantial fraction of the eddy kinetic energy. This result along with the observed time scales are used to assess the numerical simulations. The latter may be expected

to show some sensitivity to the bottom friction and viscosity coefficients; however, no attempt has been made to tune these parameters to improve the results. The approach adopted here is to study the effects of wind forcing and bottom topography given a reasonable set of model parameters.

The parameters of the numerical experiments considered below are listed in Table 5. The focus of these experiments is on the influence of the wind forcing and bottom topography on characteristics of the variability. For experiment FNOC-T, a daily wind-stress curl field, derived from FNOC synoptic analyses for the period 1975-87, was used to drive the model. [A portion of the velocity time series obtained from this experiment is shown in Fig. 10 of Cummins (1991).] In two experiments, M-F and M-T, the model is forced with a mean wind-stress curl field that is derived from an average over the 13 years of FNOC winds.

In other experiments, the wind forcing is represented by a stochastic wind-stress curl field. This type of forcing is used to represent the random torques applied to the ocean due to mesoscale atmospheric fluctuations. Large et al. (1991) have shown that most of the variance in the wind-stress curl north of 40°N in the North Pacific is associated with this type of forcing. The stochastic wind forcing is implemented with a Markovian process (Treguier and Hua 1987; Cummins 1991) and is characterized by a constant isotropic-wavenumber spectrum with maximum and minimum forced wavelengths denoted in Table 5 by L_{\max} and L_{\min} , respectively. The one-sided frequency spectrum $F(\omega)$ of the Markovian process is

$$F(\omega) = \frac{W_0}{[T_F \omega]^2 + 1}, \quad (3.17)$$

where

$$W_0 = \frac{2T_F \langle S^2 \rangle}{\pi} \quad (3.18)$$

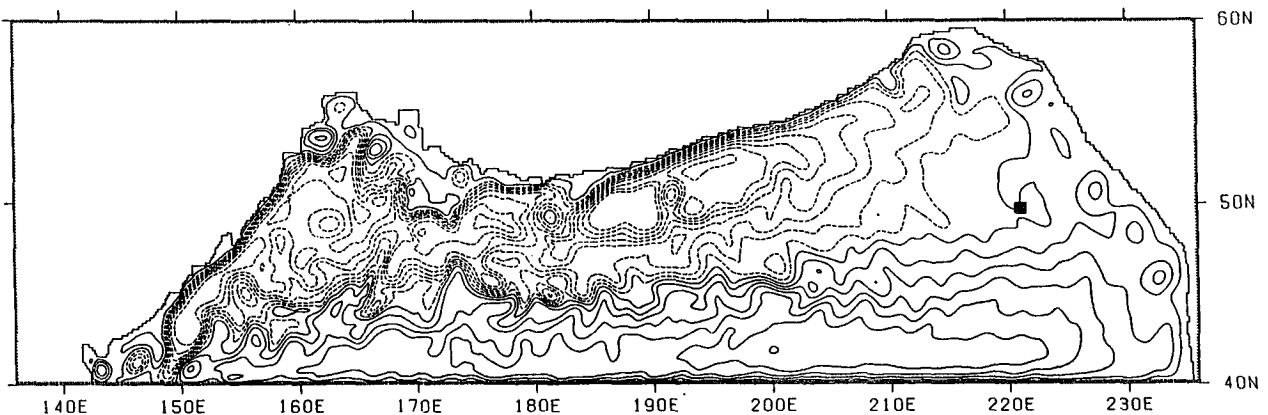


FIG. 7. Instantaneous streamfunction field of the top layer from experiment FNOC-T (Table 5). The contour interval is $7500 \text{ m}^2 \text{ s}^{-1}$. Note the presence of the Alaskan Stream as a coherent flow along the slanting northern boundary, which separates from the coast at about 185°E . The solid square indicates the location of the LP10-1 mooring.

TABLE 5. Parameters of the numerical experiments. In the topography heading, NP stands for the ETOPO5 topography of the North Pacific, while F stands for a flat bottom. In the forcing heading, FNOC stands for daily FNOC winds (1975–87), M stands for mean winds derived from a 13-year time average of the FNOC winds and S stands for a stochastic wind forcing. Where applicable, the parameters of the stochastic wind field are given. The final column gives the averaging period used in the computation of statistics.

Experiment	Topography	Forcing	W_0 ([N m ⁻³] ² Hz ⁻¹)	L_{\min} (km)	L_{\max} (km)	Period (years)
FNOC-T	NP	FNOC				5
M-F	F	M				2
M-T	NP	M				2
S-F	F	S	2×10^{-7}	400	4000	6
S-T	NP	S	2×10^{-7}	400	4000	6
S2-F	F	S	2×10^{-7}	200	4000	6
S2-T	NP	S	2×10^{-7}	200	4000	6
S3-T	NP	S	4×10^{-7}	400	4000	6
SM-T	NP	S + M	2×10^{-7}	400	4000	4

is the white noise level, and $\langle S^2 \rangle$ is the variance of the wind-stress curl. For periods longer than the integral time scale T_F , the frequency spectrum is white, while for shorter periods the spectrum falls off as ω^{-2} . With a proper choice of parameters, the Markovian process yields a frequency-wavenumber spectrum that retains the main aspects of the observed wind-stress curl spectrum (Treguier and Hua 1987). The white noise level W_0 is varied between 2×10^{-7} and 4×10^{-7} [N m⁻³]² Hz⁻¹. In comparison, Large et al. (1991) analyzed seven years of twice-daily synoptic winds with 2.5° resolution from the ECMWF atmospheric model, and obtained a mean annual white noise level of 1.6×10^{-7} [N m⁻³]² Hz⁻¹ at 50°N, 180°. An integral time scale of 10 days is selected for the stochastically forced experiments. With these parameters the stochastic forcing has a variance which is comparable to that of the FNOC wind-stress curl over the northeast Pacific. An isotropic forcing, constant over all forced scales, is only an approximation to the actual forcing, where the large scales are generally more energetic (Large et al. 1991).

c. Results

The principal results from the numerical experiments are summarized in Tables 6 and 7. The most

realistically configured experiment is FNOC-T, which is forced with “real” winds and includes the bottom topography. Statistics computed from the velocity data of this experiment are in reasonable agreement with observations. There is an approximate equipartition of energy between the barotropic and first baroclinic mode, and the level of depth-integrated K_E , though underestimating the measurements by about 40% is nevertheless within the correct range. Also in agreement with observations is the marked variation in the time scales of the flow with depth; the surface and middle layers display long period motions while the bottom layer is characterized by a relatively high-frequency signal.

Most of the remaining experiments were conducted to determine what is essential to producing the variability observed in experiment FNOC-T. In two experiments, M-T and M-F, the same mean wind-stress curl field as experiment FNOC-T is applied and the influence of the bottom topography is examined. In both cases, the model time series compare poorly with the data. Eddy energy levels are far too low; the currents in experiment M-T are excessively baroclinic while those of experiment M-F are too barotropic. Stick plots of the currents from experiments M-F and M-T (Fig. 8a and 8b) illustrate convincingly how poorly these

TABLE 6. The depth-integrated eddy kinetic energy (E_{KE}) in cm² s⁻² and the partition of E_{KE} among the vertical modes in the numerical experiments.

Experiment	E_{KE}	Percent		
		Mode 0	Mode 1	Mode 2
FNOC-T	0.75	45	48	7
M-F	0.14	79	16	5
M-T	0.28	9	81	10
S-F	1.29	92	7	1
S-T	0.31	67	27	6
S2-F	0.67	61	34	5
S2-T	0.22	36	57	7
S3-T	0.78	61	35	4
SM-T	0.58	44	45	11

TABLE 7. The eddy kinetic energy (K_E) in cm² s⁻² at the mooring location in the numerical experiments. Values at middepth of the three layers of the model are given.

Experiment	K_E at		
	100 m	500 m	2900 m
FNOC-T	9.5	1.0	0.3
M-F	0.7	0.2	0.1
M-T	5.6	0.4	0.0
S-F	2.9	1.5	1.2
S-T	2.4	0.3	0.2
S2-F	5.5	0.9	0.4
S2-T	2.9	0.4	0.1
S3-T	6.4	1.1	0.5
SM-T	7.2	0.9	0.2

experiments compare with the observations. The motions in experiment M-F are characteristic of a baroclinically unstable flow and the associated deep-current fluctuations have a relatively long, $O(100)$ -day, period. The topography in experiment M-T stabilizes the flow but yields very weak currents in the deep layer. This is the reason for the very low level of barotropic eddy energy. The situation in the northeast Pacific is apparently quite different from the western Pacific where Schmitz and Holland (1986) found that a quasigeostrophic model forced with steady winds could account for the abyssal eddy kinetic energy in the Kuroshio extension region.

As suggested by (3.14), the low-frequency forcing in M-T produces predominantly baroclinic motions. In the case of experiment M-F, the barotropic mode fluctuations are due to nonlinear processes, and a linear relation such as (3.14) is no longer applicable. A preliminary experiment, with a different mean wind-stress curl forcing derived from the Hellerman and Rosen-

stein (1982) winds, failed to develop the instability obtained at the mooring location in experiment M-F, presumably because the mean wind-stress curl field from Hellerman and Rosenstein is somewhat weaker than the one from the FNOC winds. In this case, the K_E distribution among the modes is similar to M-F, with about 85% of the energy in the first baroclinic mode, in accordance with (3.14).

The results from experiments M-F and M-T demonstrate the inadequacy of specifying only the steady component of the wind field. To contrast with this, several experiments were conducted with the stochastic forcing discussed in the previous section. The daily FNOC winds of course contain fluctuating component of the wind-stress curl as well as the mean component. In experiment S-F, a flat-bottom ocean is forced with a stochastic wind using a standard set of parameters. The level of eddy energy in experiment S-F is comparable to the observations. In particular, the stochastic forcing produces a realistic level of eddy energy in the deep layer, in contrast to the steadily forced cases; however, an unrealistic aspect of experiment S-F is that almost all of the eddy energy is in the barotropic mode. The situation in experiment S-F is similar to the one discussed in Treguier and Hua (1987). They found that a very large fraction of the energy in their stochastically forced flat-bottom model was in the barotropic mode, unless they restricted the forcing scales to unrealistically small values. The response in S-F is consistent with (3.15); the relatively high-frequency, large-scale wind is effective at forcing the barotropic mode. A consequence of this very strong barotropic response is the vertical uniformity of the time scales of the flow with depth. This is illustrated in the stick plot of Fig. 9a, which is visually dominated by a fast time-scale, vertically coherent response.

Experiment S-T is similar to S-F, but includes bottom topographic variations. The introduction of bottom topography leads to an increase in the fraction of first baroclinic mode K_E and to a sharp reduction in the overall depth-integrated K_E level, due mostly to a reduction in the currents of the bottom layer. In comparison with experiment M-T, the stochastic forcing, with its relatively high-frequency content, greatly increases the fraction of barotropic energy over the case with mean wind forcing. Although the depth-integrated K_E level is too low in comparison with the observations, experiment S-T is able to capture the vertical variation of the time scales of the flow that is characteristic of experiment FNOC-T and of the observations (Fig. 9b). This is associated with a lack of coherence between the upper- and lower-layer currents.

To further demonstrate the vertical variation in eddy time scales, temporal structure functions for the meridional component of velocity from experiments S-F and S-T are presented in Fig. 10. In both cases the structure functions of the bottom layers reach a saturation level over a short time lag of about 10-20 days.

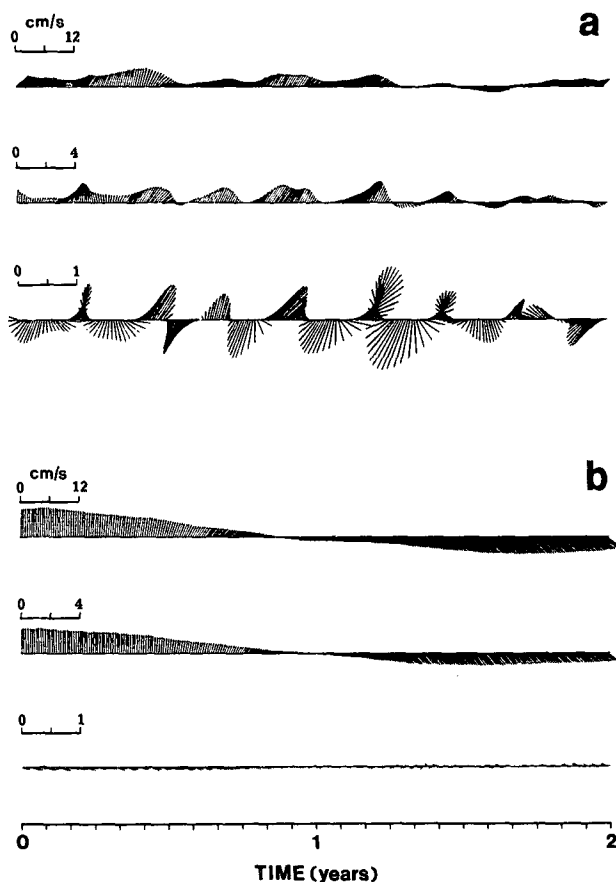


FIG. 8. Stick plots at four-day intervals of the velocity vector at $(49^{\circ}30'N, 221^{\circ}20'E)$ in different layers from two experiments with a three-layer quasigeostrophic numerical model, forced with the mean FNOC winds; (a) experiment M-F (flat bottom), (b) experiment M-T (variable-bottom topography). Each tick mark of the horizontal axis represents 30 days.

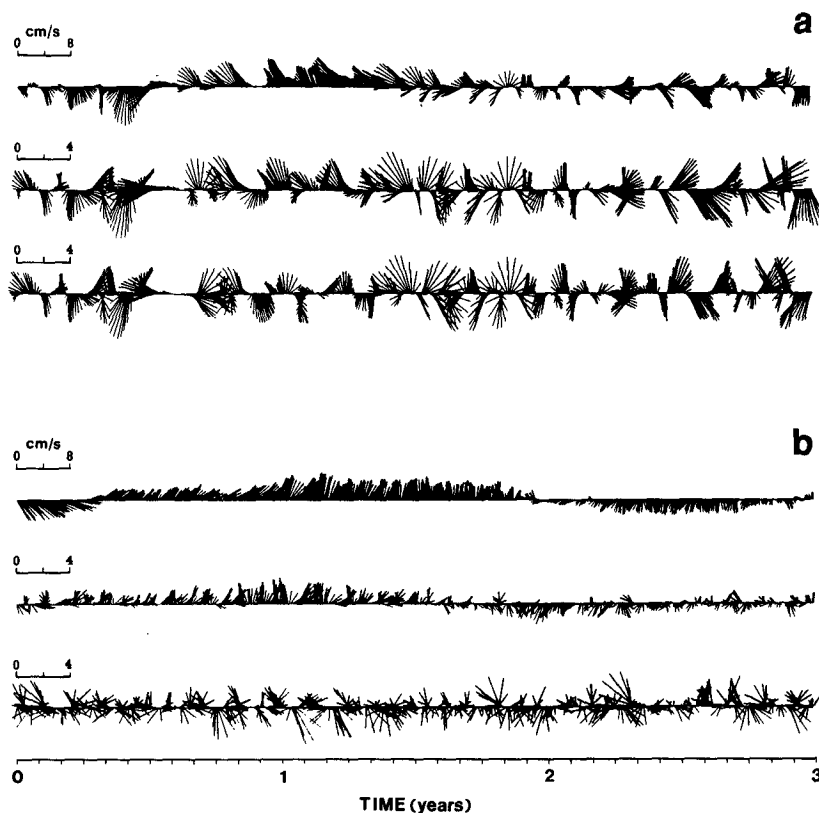


FIG. 9. As in Fig. 8; stick plots at two-day intervals of the velocity vector from two stochastically forced numerical experiments; (a) experiment S-F (flat bottom), (b) experiment S-T (variable-bottom topography).

A different behavior is obtained, however, for the uppermost layer. In experiment S-F, the surface-layer structure function also reaches an equilibrium level at a time lag of about 20 days, which is maintained for lags up to 100 days. In this experiment the stabilization of the surface-layer structure function at short lags is due to the relative importance of short time scales of variability in the upper layer. The presence of longer time scales is also indicated by the general increase in the structure function for lags greater than 100 days. Conversely, in S-T, the surface layer does not show an equilibrium level at short lags because fluctuations with short time scales are relatively unimportant in the upper layer.

The comparison between experiments S-F and S-T demonstrates the importance of bottom topography to the statistical properties of wind-driven variability. The changes in the modal structure of the response are qualitatively consistent with the simple bottom-slope effects discussed in section 3a. The numerical experiments confirm that the topography increases the baroclinicity of the response. The emergence of different time scales with depth is a consequence of the suppression of the barotropic mode over a range of frequencies by the topography. This permits the surface-intensified

first baroclinic mode to dominate the response over a range of low frequencies.

The relative success of experiments S-T and S-F in retaining, at least qualitatively, some aspects of the observed vertical structure motivated additional experiments with stochastic wind forcing. In S2-T and S2-F, the forced scales are extended from 400 to 200 km. Since the white noise level is unchanged, the amplitude of the forcing at scales greater than 400 km is substantially reduced from experiment S-T. The relations derived from linear theory, (3.13) and (3.15), suggest that this should lead to a shift of energy from the barotropic to first baroclinic mode. This is borne out in the numerical results; the fraction of baroclinic K_E increases considerably when the forcing is redistributed to higher wavenumbers. There is also a decrease in the level of overall depth-integrated K_E . The latter is quite sensitive to the specified white-noise level of the forcing; doubling this quantity, as in experiment S3-T, significantly increases the depth-integrated K_E .

In the final experiment listed in Table 5, SM-T, the forcing is a combination of the mean FNOC wind-stress curl with the stochastic wind. The results show that inclusion of the mean forcing also contributes to increasing the baroclinicity of the flow. The structure

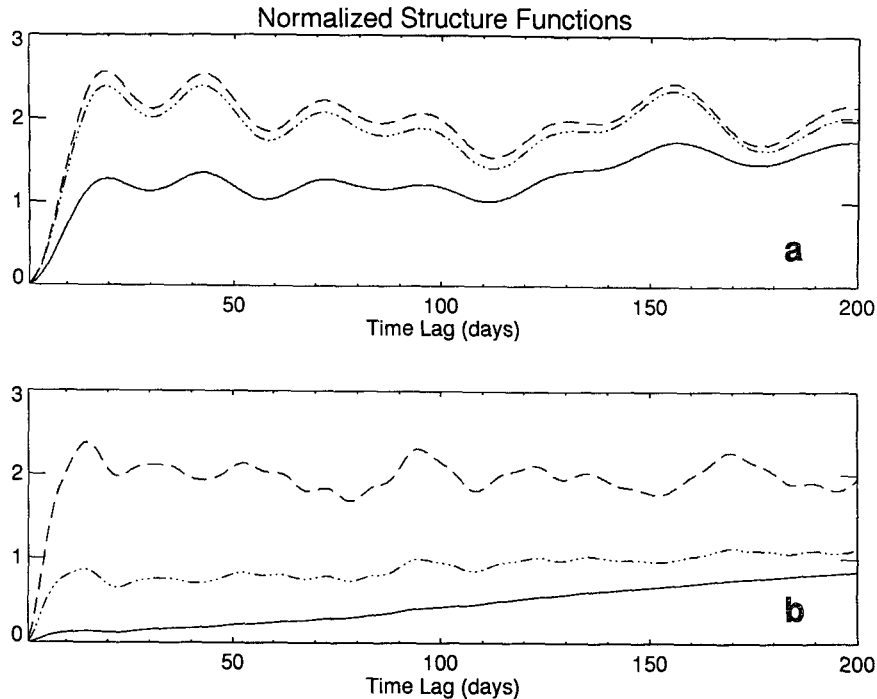


FIG. 10. Normalized temporal structure functions of the meridional velocity in each of the three layers from (a) experiment S-F and (b) experiment S-T. The solid line is for the upper layer, the dash-dotted line for the middle layer, and the dashed line for the lower layer. Note the different behavior of the upper-layer structure functions in these two experiments.

of the currents and the energy level in SM-T are similar to those of experiment FNOC-T. As in all the experiments where the first baroclinic mode is important, the flow again displays a vertical variation in the eddy time scales, with long time scales in the surface layers and short time scales at depth.

4. Summary and conclusions

We first presented a yearlong record of current meter data from a mooring LP10-1, situated in the interior of the Alaskan gyre along line P. These data constitute one of the few existing measurements of absolute velocity from the northeast Pacific. The currents are surface-intensified motions and have a characteristic vertical variation in eddy time scales; short time scales are found at 3000 m while longer time scales dominate the near-surface velocity records. Similar flow characteristics and energy levels are also found in data from the NEPAC mooring at 42°N, 152°W.

The data from the LP10-1 mooring were compared with simulated, velocity time series from a quasigeostrophic numerical model of the region. The comparison suggests that the main driving mechanism for the observed variability is the stochastic forcing of the ocean by the atmospheric winds. This is consistent with recent measurements of depth-integrated velocity from the central North Pacific (Luther et al. 1990; Chave et al. 1992) and adds further evidence to support the

premise of MF81 that direct atmospheric forcing of oceanic variability is an important generation mechanism for eddy energy over the ocean interior. The model results also provide evidence that baroclinic currents are an important component of the response to this forcing. The intensity of the response to the mesoscale wind fluctuations appears to be comparable to or greater than the intensity of the mean flow throughout the water column in the interior of the Alaskan gyre.

The model simulations and a supporting analytical calculation also indicate that the presence of topography can be important to the vertical structure of the flow. Variable bottom topography enhances the baroclinicity of the flow fluctuations and thereby contributes to the occurrence of a vertical variation in eddy time scales. This can lead to a low coherence between deep- and upper-ocean currents. Additional factors, such as the presence of a mean forcing, can also contribute to determining the baroclinicity of the flow.

Overall, the LP10-1 mooring data together with the model simulations and the NEPAC data at 42°N suggest that much of the eddy variability in the interior of the subpolar gyre in the northeast Pacific is driven by stochastic wind fluctuations. This situation may not occur further to the south in the subtropical gyre, where the variance in the wind-stress curl is much weaker (see Fig. 3 of Large et al. 1991). Accordingly, the NEPAC data from 28°N, 152°W display very different

characteristics from the 42°N and LP10-1 moorings. Niiler and Hall (1988) have shown that baroclinic instability is the dominant eddy-generation mechanism at this site.

Acknowledgments. Dr. Pearn P. Niiler graciously provided us with the NEPAC current meter data. We are grateful to Dr. D. S. Luther for the preparation of coherence maps.

REFERENCES

- Brink, K. H., 1989: Evidence for wind-driven current fluctuations in the western North Atlantic. *J. Geophys. Res.*, **94**, 2029–2044.
- Chave, A. D., D. S. Luther, and J. H. Filloux, 1992: The barotropic electromagnetic and pressure experiment. I: Barotropic current response to atmospheric forcing. *J. Geophys. Res.*, **97**, 9565–9593.
- Cummins, P. F., 1991: The barotropic response of the subpolar North Pacific to stochastic wind forcing. *J. Geophys. Res.*, **96**, 8869–8880.
- , and L. A. Mysak, 1988: A quasi-geostrophic circulation model of the northeast Pacific. Part I: A preliminary numerical experiment. *J. Phys. Oceanogr.*, **18**, 1179–1189.
- Flierl, G. R., 1978: Models of vertical structure and the calibration of two-layer models. *Dyn. Atmos. and Oceans*, **2**, 341–381.
- Frankignoul, C., and P. Müller, 1979: Quasi-geostrophic response of an infinite β -plane ocean to stochastic forcing by the atmosphere. *J. Phys. Oceanogr.*, **9**, 104–127.
- Hellerman, S., and M. Rosenstein, 1983: Normal monthly wind stress over the World Ocean with error estimates. *J. Phys. Oceanogr.*, **13**, 1093–1104.
- Hu, J. H., and P. P. Niiler, 1987: NEPAC current meter and XBT data for the circulation in the northeast Pacific thermocline: 42°N and 28°N, 152°W; July 1982–October 1985. Tech. Rep., SIO Ref. No. 87-4.
- Koblinsky, C. J., P. P. Niiler, and W. J. Schmitz, Jr., 1989: Observations of wind forced deep ocean currents in the North Pacific. *J. Geophys. Res.*, **94**, 10 773–10 790.
- Large, W. G., W. R. Holland, and J. C. Evans, 1991: Quasi-geostrophic ocean response to real wind forcing: The effect of temporal smoothing. *J. Phys. Oceanogr.*, **21**, 998–1017.
- Luther, D. S., A. D. Chave, J. H. Filloux, and P. F. Spain, 1990: Evidence for local and nonlocal barotropic responses to atmospheric forcing during BEMPEX. *Geophys. Res. Lett.*, **17**, 949–952.
- Müller, P., and C. Frankignoul, 1981: Direct atmospheric forcing of geostrophic eddies. *J. Phys. Oceanogr.*, **11**, 287–308.
- National Geophysical Data Center, 1987: ETOPO5, 5 Minute Gridded World Elevations and Bathymetry—a Digital Data Base, Boulder, Colorado.
- Niiler, P. P., and M. M. Hall, 1988: Low-frequency eddy variability at 28°N, 152°W in the eastern North Pacific subtropical gyre. *J. Phys. Oceanogr.*, **18**, 1670–1685.
- Rhines, P. B., 1970: Edge-, bottom-, and Rossby waves in a rotating stratified fluid. *Geophys. Fluid Dyn.*, **1**, 273–302.
- , 1977: The dynamics of unsteady currents. *The Sea*. Vol. 6, E. D. Goldberg, I. N. McCane, J. J. O'Brien, and J. H. Steele, Eds. Wiley Interscience, 189–318.
- Samelson, R. M., 1989: Stochastically forced current fluctuations in vertical shear and over topography. *J. Geophys. Res.*, **94**, 8207–8215.
- , 1990: Evidence for wind-driven current fluctuations in the eastern North Atlantic. *J. Geophys. Res.*, **95**, 11 359–1168.
- Schmitz, W. J., and W. R. Holland, 1986: Observed and modeled mesoscale variability near the Gulf Stream and Kuroshio extension. *J. Geophys. Res.*, **91**, 9624–9638.
- Tabata, S., 1991: Annual and interannual variability of baroclinic transports across Line P in the northeast Pacific Ocean. *Deep-Sea Res.*, **38**, S221–245.
- , and J. L. Peart, 1986: Statistics of oceanographic data based on hydrographic/STD casts made at Stations 7 through 12 along Line P during January 1959 through June 1981. *Can. Data Rep. Hydrogr. Ocean Sci. No. 43*, 402 pp.
- Thomson, R. E., P. H. LeBlond, and W. J. Emery, 1990: Analysis of deep-drogued satellite-tracked drifter measurements in the northeast Pacific. *Atmos.–Ocean*, **28**, 409–443.
- Treguier, A. M., and B. L. Hua, 1987: Oceanic quasi-geostrophic turbulence forced by stochastic wind fluctuations. *J. Phys. Oceanogr.*, **17**, 397–411.
- , and —, 1989: Influence of bottom topography on stratified quasi-geostrophic turbulence in the ocean. *Geophys. Astrophys. Fluid Dyn.*, **43**, 265–305.
- Willebrand, J. S., G. H. Philander, and R. C. Pacanowski, 1980: The oceanic response to large scale atmospheric disturbances. *J. Phys. Oceanogr.*, **10**, 411–429.